Available online at www.sciencedirect.com
ScienceDirect
International Journal of Heat and Mass Transfer 51 (2008) 4083–4094
International Journal of HEAT and MASS TRANSFER
www.elsevier.com/locate/ijhmt

Prediction of the temperature field in flat plate heat pipes with micro-grooves – Experimental validation

Frédéric Lefèvre *, Romuald Rullière, Guillaume Pandraud, Monique Lallemand

CETHIL, UMR 5008 CNRS-INSA-UCB, INSA-Lyon, 20 av. A. Einstein, F-69621 Villeurbanne Cedex, France

Received 2 February 2007; received in revised form 12 September 2007
Available online 20 February 2008

Abstract

A liquid and vapour flow model coupled to a thermal model is presented for a flat plate heat pipe with micro-grooves. This model allows the calculation of the liquid and vapour pressures and velocities, the meniscus curvature radius in the grooves and the temperature field in the heat pipe wall from the heat source to the heat sink. The meniscus curvature radius is introduced in the thermal model to take into account the heat transfer at the liquid–vapour interface. Experimental measurements of the meniscus curvature radius as well as temperature measurements along a grooved heat pipe are compared to the model results. Both comparisons show the good ability of the numerical model to predict the maximum heat transport capability and the temperature field in the heat pipe. The model is used to optimize the heat pipe dimensions in order to improve its thermal performances.

Keywords: Flat plate heat pipe; Two-phase heat spreader; Meniscus curvature; Heat transport capability; Thermal resistance; Micro-grooves

1. Introduction

Flat plate heat pipes are micro-fluidic devices that are usually designed for the thermal management of electronic components [1]. They are used for their heat transport capacity as well as their high level of uniform temperature distribution. This is the reason why these cooling devices are also qualified of two-phase heat spreader (TPHS).

Recently, Rullière et al. [2,3] have tested a micro-grooved TPHS for the cooling of proton exchange membrane fuel cells (PEMFC). This application aims at reducing the cooling system volume and homogenizing the temperature in the core of fuel cells, where the working temperatures range between 60 °C and 100 °C. The heat production inside the PEMFC is about 0.5 W cm^{-2} and has to be removed from important areas (200–1000 cm^2). Unlike classical TPHS applications, PEMFC cooling involves a big heat source, a small heat sink and a small adiabatic region. Rullière et al. [2,3] have tested such a copper flat TPHS with a wide evaporating area (190×90 mm^2) compared to the condenser area (30×90 mm^2). The experimental results show that TPHS are very efficient systems for PEMFC cooling. In both vertical favourable orientation and horizontal orientation, the temperature difference is lower than 1.6 K on the entire evaporator surface area for a heat transfer rate equal to 85 W (0.5 W cm^{-2}) and a working temperature of 70 °C.

In horizontal orientation, a confocal microscope was used to measure the meniscus curvature radius along the grooves when the liquid motion is due to capillary forces rather than to volume forces. A two-phase flow model was developed to calculate the meniscus curvature radius, the liquid and vapour pressures and the liquid and vapour velocities along the TPHS. The comparison between the experimental data and the model results shows the good ability of the numerical model to predict the meniscus curvature radii from which the maximum heat transport capability of the TPHS is depending.

A hydrodynamic model allows calculating the capillary heat transport limitation but is not sufficient to

* Corresponding author. Tel.: +33 4 7243 8251; fax: +33 4 7243 8811.
E-mail address: frederic.lefevre@insa-lyon.fr (F. Lefèvre).

0017-9310/$ - see front matter © 2008 Elsevier Ltd. All rights reserved.
doi:10.1016/j.ijheatmasstransfer.2007.12.007

Nomenclature

a	accommodation coefficient
A	cross-section area (m^2)
c	aspect ratio
f	friction coefficient
g	gravitational acceleration ($m\ s^{-2}$)
h	heat transfer coefficient ($W\ m^{-2}\ K^{-1}$)
H	height (m)
h_{lv}	latent heat of vaporisation ($J\ kg^{-1}$)
i	node number
K	meniscus curvature (m^{-1})
l	width (m)
L	length (m)
$\overline{M}$	mass per mole ($kg\ mol^{-1}$)
n	total node number
P	pressure (Pa)
Po	Poiseuille number
q	heat flux ($W\ m^{-2}$)
Q	heat transfer rate for a control volume (W)
r	meniscus curvature radius (m)
R	thermal resistance ($K\ W^{-1}$)
$\overline{R}$	ideal gas constant ($J\ K^{-1}\ mol^{-1}$)
Re	Reynolds number
S	surface area (m^2)
T	temperature (K)
T_0	temperature at $y = H_w + H_g + H_v/2$ (K)
u	velocity along the z-axis ($m\ s^{-1}$)
v	velocity along the y-axis ($m\ s^{-1}$)
w	velocity along the x-axis ($m\ s^{-1}$)
x, y, z	coordinates (m)

Greek symbols

α	angle (rad)
δ	film thickness (m)
δ'	film thickness derivative
φ	transversal heat flux ($W\ m^{-2}$)
λ	thermal conductivity ($W\ m^{-1}\ K^{-1}$)
μ	dynamic viscosity (Pa s)
ρ	density ($kg\ m^{-3}$)
θ	contact angle (rad)
σ	surface tension ($N\ m^{-1}$)
τ	shear stress ($N\ m^{-2}$)

Subscripts

cond	condenser
evap	evaporator
f	fin
f + g	fin + groove
g	groove
hs	heat sink
i	node number
int	interfacial
l	liquid
long	longitudinal
max	maximum
min	minimum
sat	saturation
trans	transversal
v	vapour
w	wall

characterize the thermal performances of a TPHS. The effective thermal conductivity must also be investigated to determine the relationship between the temperature field and the input power. Therefore, a thermal model has to be developed to calculate the temperature field and the thermal resistance of the device.

Several authors have developed both hydrodynamic and thermal models of grooved TPHS [4–7]. In [4], an analytical solution for the liquid and the vapour flows coupled to an analytical solution for the wall temperature was presented. This model can be used when several heat sources and heat sinks are located on a flat heat pipe and for different capillary structures such as meshes or sintered powder wick. Nevertheless, the permeability and the equivalent thermal conductivity of the capillary structure are considered to be constant, which is not well adapted to grooves. Indeed, the variation of the liquid thickness that occurs along the grooves affects the liquid film resistance and the cross-section of both the vapour and the liquid flows.

The hydrodynamic models developed in [5–7] are based on the balance equations and the Young Laplace law. The flow equations are coupled to thermal models of the evaporator and the condenser. In [5,6], 1D thermal models were developed. Jiao et al. [7] developed a 2D approach and put forward the influence of the contact angle, the groove configuration and the film condensation on the temperature drop from the heat source to the heat sink. The evaporator model includes the effect of the evaporating thin film region [8]. However, axial heat conduction in the wall is not taken into account, whereas it could affect TPHS thermal performances [4], mainly when the adiabatic area is very small.

In the present work, a thermal model is developed and coupled to the hydrodynamic model already presented in [2]. The liquid and vapour pressures and velocities, the meniscus curvature radius in the grooves and the temperature field in the TPHS wall are calculated from the heat source to the heat sink. The meniscus curvature radius, calculated in the two-phase flow model, is taken into account to model the heat transfer by heat conduction and phase change inside the TPHS. The thermal and the hydrodynamic models are validated with both temperature and meniscus curvature radius measurements. Several works have already shown the influence of the meniscus curvature radius on the temperature field along a grooved heat pipe. However, it was only validated experimentally by temperature measurements. The scoop of the present investigation

is to associate local temperature measurements to measurements of the meniscus curvature radius in the grooves. The validated model is then used to find the optimal dimensions of the TPHS.

2. Capillary two-phase flow model

The TPHS under investigation is presented in Fig. 1. It consists of a long grooved plate with a single flat vapour channel. The grooves, whose cross-section is rectangular of height H_g and width l_g, are separated by fins of width l_f. The wall thickness under the grooves is H_w and the vapour space height H_v. The axial coordinate z is equal to zero at the evaporator beginning and to L at the condenser end. The evaporation and condensation lengths are longer than the heat source and heat sink lengths, respectively, due to heat conduction in the wall. The transversal coordinate y is equal to zero at the middle of the TPHS. The heat sources and the heat sinks, placed each one at an extremity of the TPHS, are separated by a short adiabatic area. They are located on both the TPHS top and base and occupy all the TPHS width. Thus, the configuration is symmetrical in height and in width and it is possible to take into account only half a groove, half a fin and half a vapour space to model the TPHS. The model can be applied to any type of grooves with cross-sections such as trapezoidal or triangular.

The capillary two-phase flow model is one-dimensional and steady-state. It is based on previous works on micro-heat pipes arrays [9–11] and was modified for TPHS. The liquid and vapour pressures, the liquid and vapour velocities and the meniscus radius are calculated all along a groove. The model also predicts the capillary limit. The equations, already presented in [2], have been modified to be coupled to the thermal model.

2.1. One-dimensional two-phase flow model

The TPHS is divided into several control volumes of length dz, height $(H_v/2 + H_g)$ (Fig. 2) and width $l_{f+g}/2$ ($l_{f+g} = l_f + l_g$) for which the balance equations are written

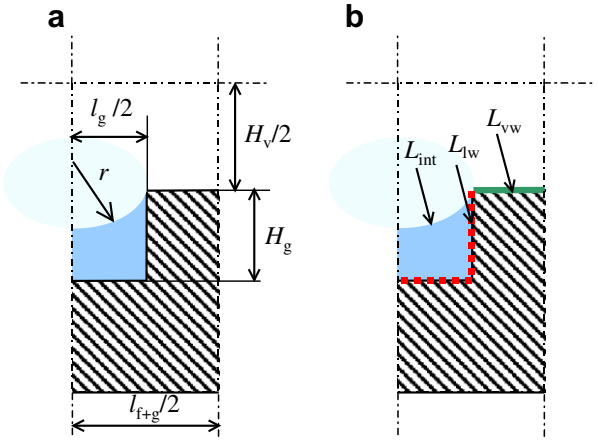

Fig. 2. Transversal cross-section of a control volume; (a) Geometrical parameters and (b) Vapour-wall and liquid-wall wetted lengths and liquid–vapour interfacial length.

for the liquid and vapour phases. For the liquid and vapour mass balance, we obtain

$$\frac{d(A_l u_l)}{dz}\,dz = L_{int} v_{int}\,dz \tag{1}$$

$$\frac{d(A_v u_v)}{dz}\,dz = \frac{\rho_l}{\rho_v} L_{int} v_{int}\,dz \tag{2}$$

where subscripts l and v denote the liquid and the vapour, respectively. A is the cross-section, L_{int} is the liquid–vapour interfacial length, z is the axial coordinate, u is the fluid velocity and ρ its density. The interfacial velocity of condensation or evaporation v_{int} is calculated from the energy balance

$$v_{int} = -\frac{\varphi(z)\frac{l_{f+g}}{2}}{\rho_l h_{lv} L_{int}} \tag{3}$$

where $\varphi(z)$ is the transversal heat flux, calculated with the thermal model and h_{lv} is the latent heat of vaporisation. Two additional equations are obtained from the momentum balance equations

$$\rho_l \frac{d(A_l u_l^2)}{dz}\,dz = -A_l \frac{dP_l}{dz}\,dz + \frac{dA_l}{dz}(P_v - P_l)\,dz + |\tau_{lw}| L_{lw}\,dz + |\tau_{int}| L_{int}\,dz - \rho_l g A_l \sin\alpha\,dz \tag{4}$$

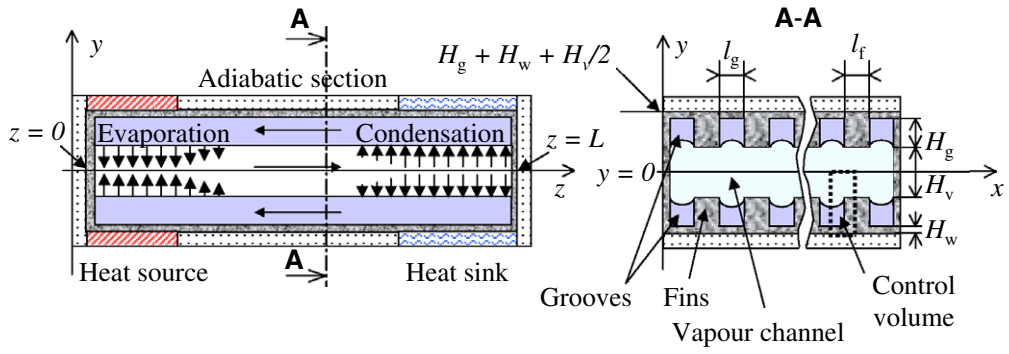

Fig. 1. Schematic of a TPHS with rectangular grooves.

$$\rho_v \frac{d(A_v u_v^2)}{dz}\,dz = -A_v \frac{dP_v}{dz}\,dz + \frac{dA_v}{dz}\,(P_l - P_v)\,dz + |\tau_{vw}|L_{vw}\,dz + |\tau_{int}|L_{int}\,dz - \rho_v g A_v \sin\alpha\,dz \quad (5)$$

where P is the pressure, τ_{lw} and τ_{vw} the liquid-wall and vapour-wall shear stresses and τ_{int} is the interfacial shear stress. L_{vw} and L_{lw} are the vapour-wall and liquid-wall wetted lengths in the control volume, respectively. The last term in Eqs. (4) and (5) is due to the body forces, α being the TPHS tilt angle in relation to the gravity field g.

The wall shear stresses are calculated by assuming liquid and vapour laminar flows

$$\tau = \frac{1}{2}\rho u^2 f \quad \text{with} \quad f = \frac{Po}{Re} \quad (6)$$

where f is the friction coefficient, Po the Poiseuille number and Re the Reynolds number. For a rectangular groove, the Poiseuille number can be calculated using the Shah and London law [12] for the liquid and the vapour

$$Po = 24\left(1 - 1.3553c_{min} + 1.9467c_{min}^2 - 1.7012c_{min}^3 + 0.9564c_{min}^4 - 0.2537c_{min}^5\right) \quad (7)$$

where c_{min} is the minimum aspect ratio between the height and the width of the cross-section. The interfacial shear stress is a parameter that is difficult to estimate. Some authors have developed expressions to cope with this parameter [13,14]. In [2], the model has been validated with experimental data obtained with a TPHS having a very small adiabatic area and it has been shown that, when phase change phenomena occur nearly all along the grooves, the interfacial shear stress is negligible.

In Eqs. (1)–(5), A_l, A_v, L_{vw}, L_{lw}, and L_{int} depend on the groove geometry and on the meniscus curvature radius r, which is calculated by deriving the Laplace–Young equation with respect to z

$$\frac{dP_l}{dz} = \frac{dP_v}{dz} - \frac{d}{dz}\left(\frac{\sigma}{r}\right) \quad (8)$$

where σ is the surface tension.

2.2. Boundary conditions

Eqs. (1)–(5) and (8) form a set of six equations, including five coupled differential equations. The resulting set of first order, non-linear, coupled ordinary differential equations is solved numerically with a fourth order Runge–Kutta method using the following boundary conditions:

$$u_l|_{z=L} = u_v|_{z=L} = 0 \qquad P_l|_{z=L} = P_{sat} - \frac{\sigma}{r|_{z=L}} \quad P_v|_{z=L} = P_{sat} \quad (9)$$

where L is the groove length and P_{sat} is the saturation pressure.

The value of $r|_{z=L}$ depends on the heat transfer rate and on the fluid fill charge. When the TPHS does not work, the meniscus curvature radius is constant all along a groove and equal to r_0. In operating conditions, it decreases or increases in the evaporator and condenser zones due to evaporation or condensation, respectively. It is assumed that in operating conditions r remains constant at the coordinate z_0 corresponding to the section where no phase change occurs. The value of $r|_{z=L}$ is obtained when the calculated meniscus curvature radius is equal to r_0 at $z = z_0$ through a shooting method on parameter r.

The maximum heat transfer rate Q_{max} is obtained when the meniscus curvature radius reaches the minimum value r_{min} [12] at $z = 0$

$$r_{min} = \frac{l_g}{2\cos\theta} \quad (10)$$

where l_g is the groove width and θ the contact angle between the meniscus and the wall.

In this model, we consider only the case were the line of contact is at the upper edge of the corner of the fin in the evaporator. The meniscus recession from the top to the bottom of the groove in the evaporator section that occurs before the dry out of the evaporator, is not taken into account here.

3. The nodal thermal model

The TPHS wall is divided into several control volumes for which the energy balance equation is written. The wall temperature T_i is calculated in each control volume i (Fig. 3). At $z = 0$ and $z = L$, the heat flux is assumed to be equal to zero in the axial direction. The boundary conditions at $y = H_w + H_g + H_v/2$ are expressed as

- an uniform heat transfer rate imposed on the TPHS wall in the heat source surface area;
- a zero heat flux in the adiabatic section;
- a Fourier boundary condition in the heat sink surface area.

For a control volume, three thermal resistances are considered to model heat transfer in the TPHS.

A transversal thermal resistance, $R_{i,trans}$ is used to model heat transfer by heat conduction and phase change in the y

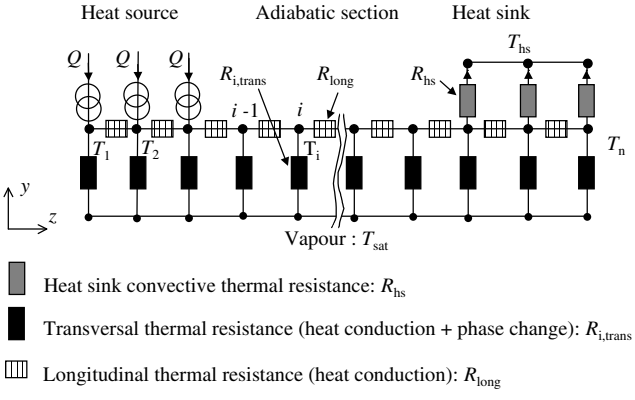

Fig. 3. The thermal node network.

direction at node i. This thermal resistance changes at each node i, which is due to the variation of the meniscus curvature radius along z and to the phase change (condensation or evaporation) that occurs in the considered control volume. The transversal thermal resistance calculation is described in Section 3.2 for the evaporator and in Section 3.3 for the condenser. The vapour temperature is assumed to be equal to the saturation temperature T_{sat} all along a groove.

R_{hs} and T_{hs} are the convective thermal resistance and the temperature of the heat sink, respectively. R_{hs} is calculated by considering the convective heat transfer coefficient of the heat sink h_{hs}. R_{long} is the longitudinal thermal resistance of the wall, which is constant all along the grooves.

By writing the energy balance, we obtain the following equations at node i:

Heat source section

$$\frac{T_{i-1}+T_{i+1}}{R_{long}} - T_i\left(\frac{2}{R_{long}}+\frac{1}{R_{i,trans}}\right)+\frac{T_{sat}}{R_{i,trans}}+Q=0$$

Adiabatic section

$$\frac{T_{i-1}+T_{i+1}}{R_{long}} - T_i\left(\frac{2}{R_{long}}+\frac{1}{R_{i,trans}}\right)+\frac{T_{sat}}{R_{i,trans}}=0$$

Heat sink section

$$\frac{T_{i-1}+T_{i+1}}{R_{long}} - T_i\left(\frac{2}{R_{long}}+\frac{1}{R_{i,trans}}+\frac{1}{R_{hs}}\right)+\frac{T_{sat}}{R_{i,trans}}+\frac{T_{hs}}{R_{hs}}=0 \quad (11)$$

Q is the heat transfer rate imposed on the TPHS wall for one control volume in contact with the heat source. By taking into account the n nodes, we obtain a set of n equations and $n+1$ unknowns: the temperature at each node and T_{sat}. The set of equations makes a tridiagonal matrix, which is solved readily. T_{sat} is calculated through an iterative process, until the evaporating heat transfer rate is equal to the condensing heat transfer rate.

The transversal heat flux $\varphi(z)$ that is used in the hydrodynamic model is expressed as

$$\varphi(z)=\varphi(i)=\frac{(T_i-T_{sat})}{R_{i,trans}\frac{l_{f+g}}{2}\,dz} \quad (12)$$

3.1. The longitudinal thermal resistance

A longitudinal thermal resistance, R_{long} allows the heat transfer calculation through the wall in the z direction

$$R_{long}=\frac{dz}{\lambda_w A_w};\quad A_w=H_w l_{f+g}+H_g l_f \quad (13)$$

where λ_w is the wall thermal conductivity and A_w is the wall cross-section in the z direction. The heat conduction in the liquid in the z direction is neglected because the thermal conductivity of the liquid λ_l is much lower than λ_w. Indeed, the usual materials for TPHS are copper, aluminium or silicon, which have high thermal conductivities. Thus, R_{long} is constant all along a groove.

3.2. The evaporator 2D thermal model

In the evaporator section, defined by a wall temperature greater than T_{sat}, the transversal thermal resistance at node i, $R_{i,trans}$ is calculated using a 2D thermal model (Fig. 4). A constant heat transfer rate Q is applied at $y=H_w+H_g+H_v/2$. At the fin top the heat flux is assumed to be equal to zero, because the convection heat transfer between the wall and the vapour is negligible compared to the evaporation heat transfer. The heat transfer is equal to zero on the vertical boundaries of the control volume because of the symmetries. As the liquid thickness and the liquid velocity are small, liquid convection is neglected in the grooves and heat transfer in the liquid is modelled by 2D heat conduction. At the liquid–vapour interface a Fourier condition is used to model the evaporation with a heat transfer coefficient h_{evap} calculated from the gas kinetic theory [15]

$$h_{evap}=\frac{2a}{2-a}\frac{\rho_v h_{lv}^2}{T_{sat}}\frac{1}{\sqrt{2\pi\frac{\overline{R}}{\overline{M}}T_{sat}}}\left(1-\frac{P_{sat}}{2\rho_v h_{lv}}\right) \quad (14)$$

where a is the accommodation coefficient, $\overline{R}$ the ideal gas constant and $\overline{M}$ the molar mass of the fluid.

The 2D model is solved using the Matlab finite element toolbox for a control volume of the evaporator. The thermal resistance $R_{i,trans}$ is calculated by considering the difference between the saturation temperature and the calculated wall temperature at $y=H_w+H_g+H_v/2$, which is almost uniform. $R_{i,trans}$ does not depend on the value of the heat transfer rate Q applied at $y=H_w+H_g+H_v/2$ because the thermal problem is linear.

Jiao et al. [7] developed two models to calculate the heat transfer in the evaporator. The first model is 1D and takes into account the heat transfer in the thin film region at the

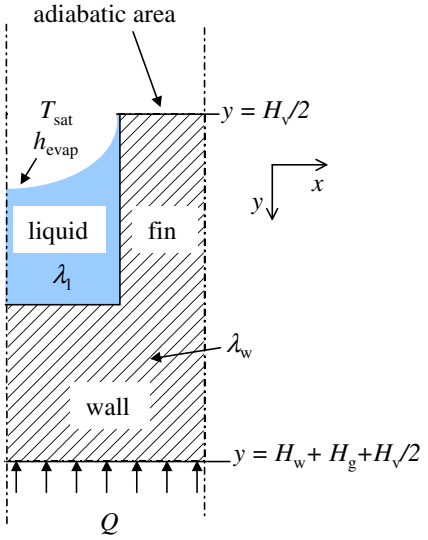

Fig. 4. Boundary conditions of a control volume in the evaporator model.

junction between the meniscus and the wall. In this region, the interface temperature cannot be assumed to be equal to the saturation temperature [16] and the shape of the liquid–vapour interface is different from the meniscus curvature radius. In the second model, the 2D heat conduction equation is solved in the liquid and the wall to calculate the heat transfer in the macro region assuming a constant temperature of the liquid–vapour interface. In the present model, a heat transfer at the liquid vapour interface is introduced in the 2D model to take into account the effect of the interface thermal resistance that acts mainly in the thin film region.

3.3. The condenser 2D thermal model

The condenser model is solved for the nodes where the wall temperature is lower than T_{sat}. Heat transfer by condensation occurs mainly on the fin top rather than in the grooves because the thermal resistance of the fins is much lower than the thermal resistance of the liquid. Indeed, the fins are generally made of a high thermal conductivity material, which is about 100 to 1000 times higher than the liquid thermal conductivity. Thus, a liquid film overlays the fin top. Depending on its thickness, the condensing film thermal resistance is not negligible and can be higher than the wall resistance. Thus, a hydrodynamic model has been developed to calculate the liquid film thickness and its thermal resistance.

3.3.1. The hydrodynamic model for the liquid film thickness calculation on the fin top

Jiao et al. [7] developed a hydrodynamic model to calculate the liquid film thickness on the fin by assuming it constant along the x-axis (Fig. 5). In the present investigation, a steady-state one-dimensional model is developed to calculate the liquid film thickness δ, the liquid pressure P_l and the liquid velocity w_l in the film, along the x-axis. This model has been adapted from a previous work developed to characterize thin evaporating films [16]. Owing to the symmetries, only one half of the fin is modelled.

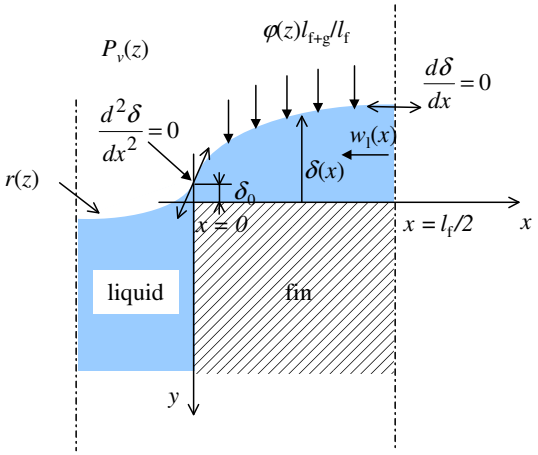

Fig. 5. Schematic of the hydrodynamic model for the condensing film thickness calculation.

The film is divided in several control volumes of length dx for which the balance equations are written. The vapour pressure is supposed to be constant all along the x-axis and equal to $P_v(z)$. The heat flux transferred to the heat sink is equal to $\varphi(z)l_{f+g}dz/2$, where $\varphi(z)$ is calculated in the thermal model (Eq. (12)). Let us assume that the vapour condensation is negligible in the grooves. Thus, the heat flux at the fin top is equal to $\varphi(z)l_{f+g}/l_f$ and the mass balance for the liquid is expressed as

$$\frac{d(\delta w_l)}{dx}dz\,dx = -\frac{1}{\rho_l h_{lv}}\varphi(z)\frac{l_{f+g}}{l_f}dz\,dx \tag{15}$$

By neglecting the liquid–vapour interfacial stress, the momentum equation is the following:

$$\rho_l\frac{d(\delta w_l^2)}{dx}dz\,dx = -\delta\frac{dP_l}{dx}dz\,dx + \tau_{lw}dz\,dx \tag{16}$$

where τ_{lw} is calculated by Eq. (6), with a hydraulic diameter for the Reynolds number equal to 2δ.

Let us introduce K the liquid film curvature

$$K = \frac{\frac{d^2\delta}{dx^2}}{\left(1+\left(\frac{d\delta}{dx}\right)^2\right)^{3/2}} \tag{17}$$

The derivative of δ with respect to x is

$$\frac{d\delta}{dx} = \delta' \tag{18}$$

By introducing Eq. (18) in Eq. (17), we obtain a first order differential equation

$$\frac{d\delta'}{dx} = K(1+(\delta')^2)^{3/2} \tag{19}$$

Owing to the Young–Laplace law, the liquid pressure on the fin top is higher than the vapour pressure

$$P_l - P_v = \sigma K \tag{20}$$

By introducing Eq. (20) in Eq. (19), we obtain

$$\frac{d\delta'}{dx} = \frac{P_l - P_v}{\sigma}(1+(\delta')^2)^{3/2} \tag{21}$$

Eqs. (15), (16), (18) and (21) make a set of four coupled first order differential equations that is solved numerically with a fourth order Runge–Kutta method.

For the boundary conditions, we assume that the meniscus curvature radius $r(z)$ is constant in a groove. Near the fin top, the liquid height is equal to δ_0 corresponding to the draining of the liquid from the fins to the groove. δ_0 is the boundary value of δ at $x=0$.

In the (x,y) coordinate system, the meniscus belongs to the circle of centre $\left(-\frac{l_g}{2};\sqrt{r^2-\frac{l_g^2}{4}}+\delta_0\right)$ and radius $r(z)$. The equation of the liquid thickness in a groove can be calculated through the circle equation with $y = H_g - \delta$

$$\left(x+\frac{l_g}{2}\right)^2 + \left(H_g - \delta - \sqrt{r^2-\frac{l_g^2}{4}} - \delta_0\right)^2 = r^2 \tag{22}$$

By deriving the equation of δ with respect to x at $x = 0$, we obtain the boundary value for δ'

$$\delta'(0) = \frac{l_g}{\sqrt{4r^2(z) - l_g^2}} \tag{23}$$

The energy balance gives the value of the liquid velocity at $x = 0$

$$w_l(0) = \frac{\varphi(z)\frac{l_{f+g}}{2}}{\rho_l h_{lv}\delta_0} \tag{24}$$

As the meniscus curvatures of the groove and the top fin are in opposite signs, the function $\delta(x)$ has an inflexion point. This inflexion point was found experimentally to be located at the edge of the fin. Thus, at $x = 0$, the meniscus curvature is equal to zero and the liquid pressure boundary condition is

$$P_l(0) = P_v(z) \tag{25}$$

As the value of δ_0 is unknown, a shooting method on parameter δ is used to calculate it. The value of δ_0 is obtained when the derivative of δ with respect to x is equal to zero on the fin symmetry axis at $x = l_f/2$.

3.3.2. Condenser 2D thermal model

Once the film thickness is known, the transversal thermal resistance at node i is calculated using a 2D thermal model (Fig. 6). A constant heat transfer rate Q is considered at $y = H_w + H_g + H_v/2$. For the calculation of the condensation heat transfer coefficient, as the physical mechanisms are similar to those of evaporation, Eq. (14) is used to calculate the heat transfer coefficient h_{cond} at the liquid–vapour interface.

The 2D model is solved using the Matlab finite element toolbox. The resulting temperature field is used to calculate the thermal resistance $R_{i,trans}$.

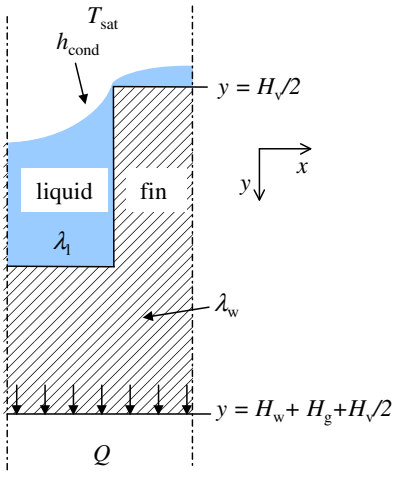

Fig. 6. Boundary conditions for a control volume of the condenser 2D model.

3.4. The hydrodynamic and thermal model coupling

The hydrodynamic and thermal models are coupled and solved in an iterative way (Fig. 7). The value of Q, T_{hs} and R_{hs} are known, as well as the heat source and heat sink surface areas. The saturation temperature is initialised at T_{hs}.

Knowing T_{sat} and $\varphi(z)$, the liquid and vapour velocities, the liquid and vapour pressures and the meniscus curvature radius are determined by the hydrodynamic model. T_{sat}, $\varphi(z)$, $r(z)$ and $P_v(z)$ allow the transversal thermal resistance calculation with the evaporator and condenser models. $R_{i,trans}$ and T_{sat} allow the calculation of the wall temperature and the transversal heat flux with the nodal thermal model. The nodal thermal model is solved several times by increasing or decreasing the saturation temperature until the total transversal heat transfer rate from the evaporator beginning to the condenser end is equal to zero. The new saturation temperature and transversal heat flux are used to solve the hydrodynamic model again. The iterative procedure is stopped when the maximum temperature difference between two iterations is lower than 0.05 K.

4. Validation with experimental data

In this section, a comparison between the model results and the experimental data presented in [2] is described. The TPHS is a long grooved TPHS with rectangular channels, similar to the one presented in Fig. 1. It is grooved only on its lower face, the upper face being sealed with a borosilicate glass plate, which allows the liquid/vapour meniscus observation in the grooves. A confocal microscope is used to locate the meniscus and to measure its curvature radius in the grooves, the TPHS being in horizontal orientation. The measurements are averaged over ten grooves located at a same z position to calculate the meniscus curvature radius. The average standard deviation of these measurements is about 50 μm.

The application of the TPHS is the cooling of proton exchange membrane fuel cells (PEMFC). Unlike classical TPHS applications, in which the heat source is small compared to the adiabatic and the heat sink regions, PEMFC cooling involves a big heat source, a small heat sink and a small adiabatic region.

4.1. Experimental set-up

The TPHS is made of 109 longitudinal micro-grooves, machined in a copper plate of area $230 \times 90\ mm^2$. The geometrical characteristics of the grooves are presented in Table 1.

The heat source is a thick resistor film of dimensions $190 \times 90\ mm^2$ located on the copper wall. The heat sink is a water heat exchanger of dimensions $30 \times 90\ mm^2$. The heat source and the heat sink are separated by a short adiabatic area of length equal to 10 mm. Two series of seven thermistors are located symmetrically along the TPHS wall and their values are averaged in each section.

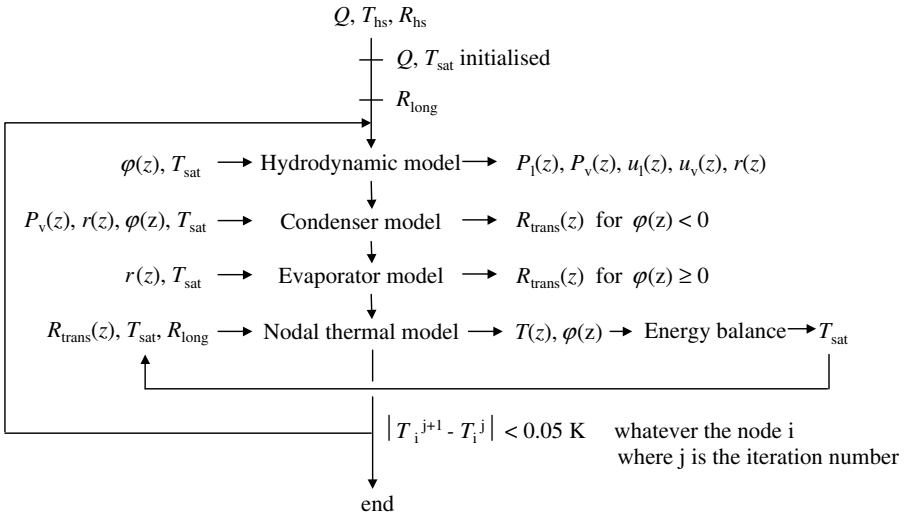

Fig. 7. Iterative process.

Table 1
TPHS characteristics

H_r	$H_v/2$	H_w	l_f	l_g	L
380 μm	1.6 mm	2 mm	400 μm	400 μm	230 mm

The TPHS is filled with methanol. The fluid load is lightly higher than the volume of the grooves, but the excess of fluid has no significant impact on the temperature field. Indeed, it remains in the corners of the condenser without flooding it.

4.2. Validation with experimental data

For the TPHS in horizontal orientation, the meniscus curvature radii have been measured all along the grooves with a confocal microscope [2]. The experimental curvature radii for imposed heat fluxes on the TPHS wall q equal to 0.5 W cm^{-2}, 0.7 W cm^{-2} and 0.9 W cm^{-2} (85.5 W, 119.7 W and 153.9 W) are shown in Fig. 8. The saturation temperature is equal to 70 °C. Dashed, solid and point dashed lines correspond to calculated radii for each heat flux, respectively. The comparison between the experimental and the calculated meniscus curvature radii shows a good agreement in the evaporator section. The difference between the measured and the calculated radii is in the range of the measurement error. In the condenser section, the difference between the experimental and the calculated results is more important. However, it has to be noticed that, in the condenser section, a small increase in the pressure difference between the liquid and the vapour leads to a high variation of the meniscus curvature radius due to the Young–Laplace law. Indeed, the more the meniscus curvature is large and the more it is sensitive to pressure variations. Thus, in the condenser, a small under-estimation or overestimation of the pressure drop leads to an important error on the meniscus curvature radius calculation.

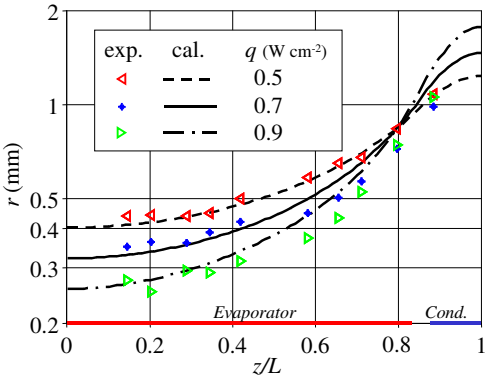

Fig. 8. Measured and calculated meniscus curvature radii along the TPHS (T_{sat} = 70 °C).

When the TPHS does not work, the measured meniscus curvature radius is equal to 850 μm all along the grooves. This value is supposed to be constant at z_0 = 187 mm (z/L = 0.81), which corresponds to the location where the calculated heat flux is equal to zero (Fig. 9). The area of condensation is larger than the heat sink area due to heat conduction in the wall.

Fig. 10 shows the comparison between the calculated and the measured temperatures along the TPHS for heat fluxes equal to 0.5 W cm^{-2}, 0.7 W cm^{-2} and 0.9 W cm^{-2}. The experimental results fit well the calculated temperatures. The temperature profile is very homogeneous on the whole evaporator area. The temperature gradients are higher in the condenser than in the evaporator, which is mainly due to a condenser area lower than the evaporator area for a same heat transfer rate. The value of the accommodation coefficient used for the calculation of the evaporation and condensation heat transfer coefficients is equal to 0.13 [17]. It leads to evaporation and condensation coefficients equal to 400 kW m^{-2} K^{-1} for T_{sat} = 70 °C. The influence of this parameter on the results is discussed later.

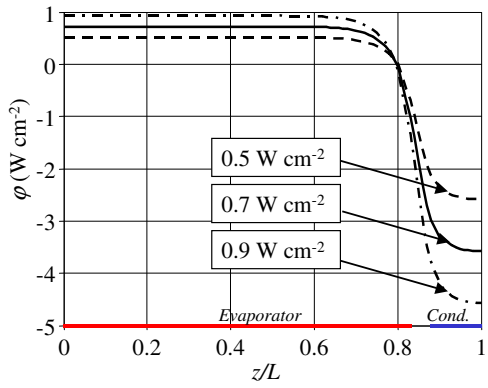

Fig. 9. Transversal heat fluxes.

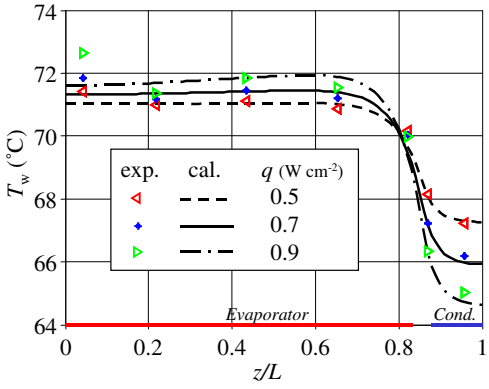

Fig. 10. Comparison between measured and calculated wall temperatures.

Fig. 11 shows heat flux vectors in a control volume located at the beginning of the evaporation area ($z/L = 0$). The transversal heat flux is transferred by conduction in the wall under the grooves. The most part of the heat flux is then transferred through the fins, until the junction of the meniscus with the wall where evaporation occurs. In the thin film region, the heat flux reaches 12 W cm^{-2} for an imposed heat flux equal to 0.5 W cm^{-2} on the outer TPHS wall.

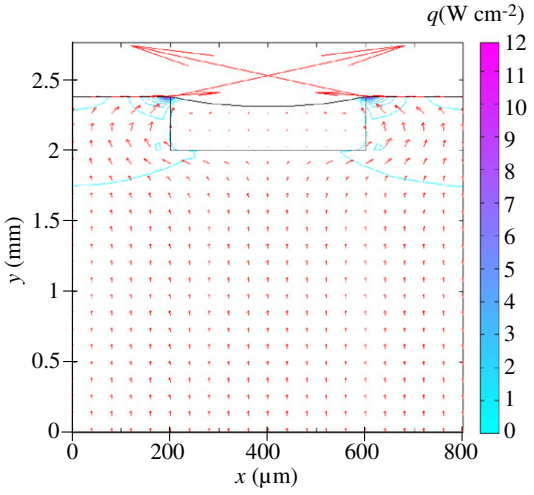

Fig. 11. Heat flux vectors in the evaporation area ($q = 0.5$ W cm^{-2}, $r = 0.4$ mm).

Fig. 12a and b shows heat flux vectors in a control volume located at the beginning ($z/L = 0.82$) and at the end ($z/L = 0.98$) of the condensation area, respectively. The heat flux transferred through the liquid in the grooves is very small. Condensation occurs mainly on the top of the fins. In the fin corner, at the junction between the meniscus curvature in the groove and the liquid film on the fin, the liquid film thickness is very small (about 1–5 μm). Thus, the heat flux transferred in this region is high. It reaches 3 W cm^{-2} at $z/L = 0.82$ and 2 W cm^{-2} at $z/L = 0.98$.

Fig. 13 shows the meniscus curvature radius and the liquid film thickness for different locations in the condenser ($z/L = 0.82$, 0.86, 0.9, 0.94, and 0.98). The liquid film thickness in the fin corner increases with the increase of the meniscus curvature radius. Therefore, the transversal thermal resistance is smaller at the beginning than at the end of the condenser.

Fig. 14 shows the transversal thermal resistance (by control volume) all along the TPHS. In the evaporation area, the most part of the heat flux is transferred at the junction of the meniscus with the fin. An increase of r leads to an increase of the liquid film thickness in this zone. Therefore, the total transversal thermal resistance increases with z. As a result, the calculated maximum temperature is obtained at $z/L = 0.7$ (Fig. 10). The discontinuity observed at $z/L \approx 0.8$ is due to the difference between evaporation and condensation mechanisms. Fig. 14 shows also that the transversal thermal resistance decreases with the increase of q in the evaporator area and increases with the increase of q in the condenser area. This can be explained by the meniscus curvature radius variation from the evaporator to the condenser.

4.3. Influence of the accommodation coefficient

Fig. 15 shows the temperatures along the TPHS for different accommodation coefficients ($q = 0.5$ W cm^{-2}). This coefficient has not a significant influence on the temperature profile shape all along the evaporator. Nevertheless, it has a strong influence on the maximal temperature difference between the evaporator and the condenser, which increases with the decrease of a. The value of a used in the model ($a = 0.13$), experimentally determined by Maerefat et al. [17], leads to a good agreement between the model and our experimental results.

5. Determination of the TPHS optimal dimensions

The model has been validated with both temperature measurements and meniscus curvature radius measurements. In this part, it is used to optimize the dimensions of the TPHS. The aim is to obtain the maximum heat transfer rate with a low thermal resistance.

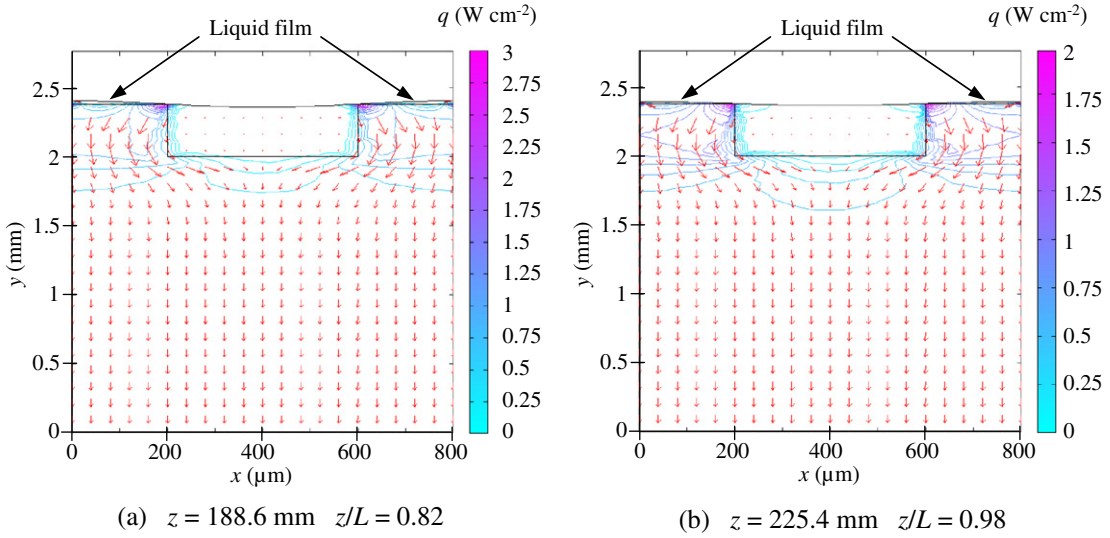

Fig. 12. Heat flux vectors in the condensation area ($q = -0.5\ \mathrm{W\,cm^{-2}}$): (a) at the beginning of the condensation area and (b) at the end of the condensation area.

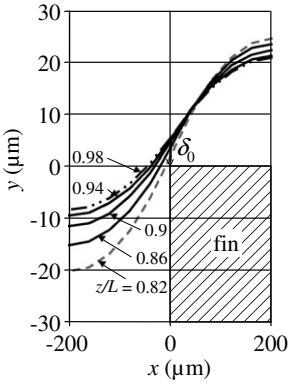

Fig. 13. Meniscus position in the condenser section at different longitudinal coordinates.

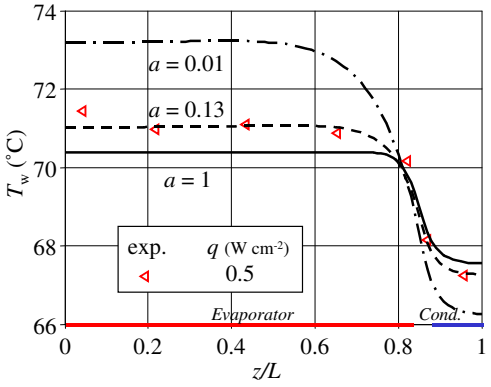

Fig. 15. Wall temperatures for different accommodation coefficients.

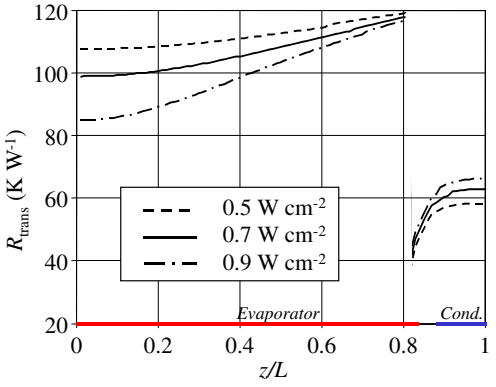

Fig. 14. Transversal thermal resistance.

The maximum heat transfer rate is obtained when the meniscus curvature radius reaches a minimum value, r_{min}, at $z/L = 0$ (Eq. (10)). It has been shown experimentally that the maximum heat transport capability, q_{max} is equal to $0.9\ \mathrm{W\,cm^{-2}}$ for T_{sat} equal to 70 °C and r_{min} equal to 257 µm (Fig. 8). The corresponding contact angle θ, equal to 39°, is supposed to remain constant to calculate r_{min} when the groove width changes.

In this study, the TPHS length, width and height are constant as well as the internal height $H_v + 2\ H_g$. The aim is to find the optimal dimensions of the grooves and of the vapour space. In this work, we consider only rectangular grooves. The effect of fin geometry is not taken into account, but it has to be noticed that this parameter can have a significant effect on the thin film evaporation and condensation [7].

5.1. Optimal groove width dimensions

Fig. 16 shows the maximum heat transport capability versus the groove width for three fin widths: $l_f = 20$ µm, $l_f = 100$ µm and $l_f = 400$ µm. When l_g increases, the liquid cross-section increases (and thus the liquid flow rate), but the capillary pressure decreases, due to a higher value of r_{min}. These opposite variations lead to an optimal value

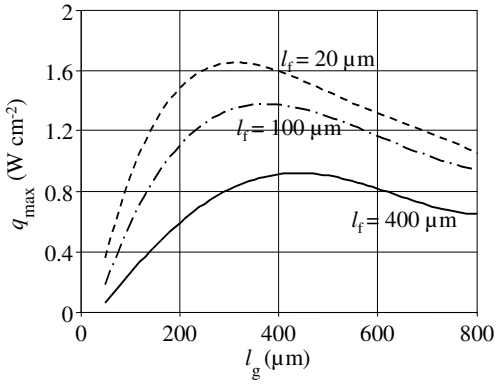

Fig. 16. Maximal heat transport capability versus the grooves width.

for l_g equal to 430 µm, 360 µm and 320 µm for l_f equal to 400 µm, 100 µm and 20 µm, respectively. When the fin width increases, the number of grooves decreases, which leads to lower performances for the same groove width.

Fig. 17 shows the thermal resistance versus the groove width for three different fin widths. The thermal resistance depends on both the number of grooves and the fin width. Many grooves enable a wide evaporation area and thus a low thermal resistance. The number of grooves depends on both l_g and l_f (Fig. 18). When l_g is small, the number of grooves is high, especially for small fins. As a result, the lowest thermal resistance is obtained for a small groove and a small fin. The number of grooves decreases with the increase of l_g and this diminution is higher for small fins than for large fins. As a result, the slope of the thermal resistance is higher for small fins than for large ones.

5.2. Optimal heights of the vapour-core and the grooves

In this study, the height of the TPHS is considered to be constant as well as the wall thickness under the grooves. Thus, the vapour-core height and the groove height are linked as follows: $H_v/2 + H_g = 1.98$ mm.

When H_g increases, the maximal heat flux increases because the liquid cross-section is larger for a same capillary pressure (Fig. 19). However, it involves the decrease

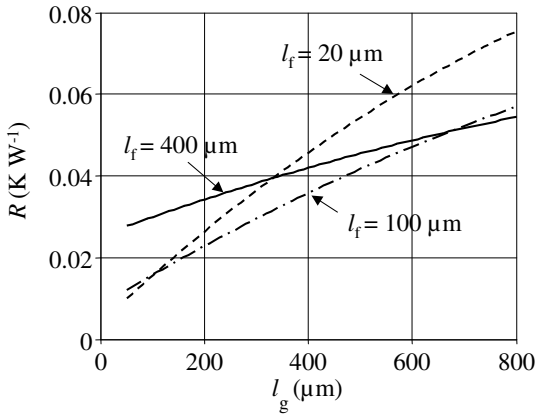

Fig. 17. TPHS thermal resistance versus the groove width.

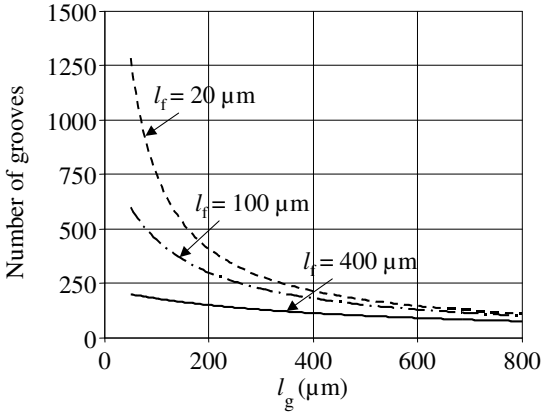

Fig. 18. Number of grooves versus the groove width.

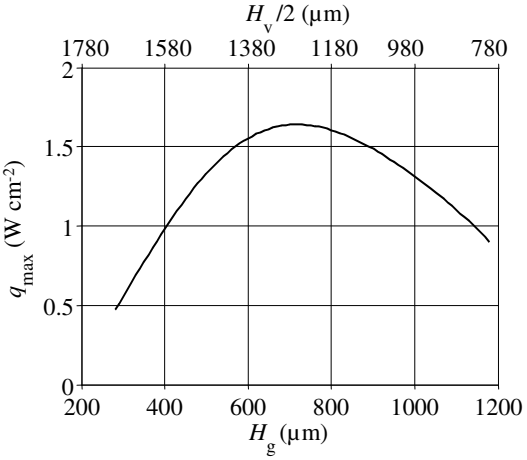

Fig. 19. Maximal heat transport capability versus the groove height.

of the vapour-core height and consequently the vapour pressure drop increases. These two opposite variations lead to an optimum ($q_{max} = 1.62$ W cm^{-2}), which is obtained for $H_v/2 = 1280$ µm and $H_g = 700$ µm. It has to be noticed that the variation of the groove height has a low influence on the thermal resistance. Indeed the fin thermal resistance is low compared to the total transversal thermal resistance. This study shows that the groove height is an important parameter that needs to be optimize to obtain a high maximum heat transport capability.

6. Conclusion

A hydrodynamic model for both the liquid and the vapour phases inside a micro-grooved TPHS coupled to a thermal model taking into account heat conduction inside the TPHS wall has been developed. These models allow the calculation of the heat transport capability of the TPHS and the temperature field in its wall. A condenser thermal model and an evaporator thermal model based on the meniscus curvature radii calculated in the hydrodynamic model have been developed to take into account the heat

transfer by phase change inside the TPHS. For the condenser, a hydrodynamic model allows the calculation of the condensation film thickness on the fins between the grooves.

The model has been validated with experimental data. Both meniscus curvature measurements and temperature measurements are compared to the numerical results. A good agreement has been found between the experimental data and the numerical results.

A parameter study has been realised to optimize the TPHS dimensions ($l_g = 360$ μm, $l_f = 100$ μm, $H_v/2 = 1280$ μm and $H_g = 700$ μm). With these dimensions, the maximal heat flux is equal to $2\ W\ cm^{-2}$ and the thermal resistance to $0.035\ K\ W^{-1}$ for $T_{sat} = 70\ °C$.

References

[1] M. Lallemand, F. Lefèvre, Micro/mini heat pipes for the cooling of electronic devices, in: 13th International Heat Pipe Conference, Shanghaï, China, 2004, pp. 12–22.

[2] R. Rullière, F. Lefèvre, M. Lallemand, Prediction of the maximum heat transfer capability of two-phase heat spreaders – Experimental validation, Int. J. Heat Mass Transfer 50 (2007) 1255–1262.

[3] R. Rullière, Etudes expérimentale et théorique de diffuseurs thermiques diphasiques – Application au refroidissement de systèmes dissipatifs, Ph.D. Thesis, INSA de Lyon, France, December 2006.

[4] F. Lefèvre, M. Lallemand, Coupled thermal and hydrodynamic models of flat micro heat pipes for the cooling of multiple electronic components, Int. J. Heat Mass Transfer 49 (2006) 1375–1383.

[5] D. Khrustalev, A. Faghri, Coupled liquid and vapor flow in miniature passages with micro grooves, J. Heat Transfer 121 (1999) 729–733.

[6] S.J. Kim, J.K. Seo, K.H. Do, Analytical and experimental investigation on the operational characteristics and the thermal optimization of a miniature heat pipe with a grooved wick structure, Int. J. Heat Mass Transfer 46 (2003) 2051–2063.

[7] A.J. Jiao, R. Riegler, H.B. Ma, G.P. Peterson, Thin film evaporation effect on heat transport capability in a grooved heat pipe, Microfluid Nanofluid 1 (2005) 227–233.

[8] H.B. Ma, P. Cheng, B. Borgmeyer, Y.X. Wang, Fluid flow and heat transfer in the evaporating thin film region, Microfluid Nanofluid (2007) (available online).

[9] J.P. Longtin, B. Badran, F.M. Gerner, A one-dimensional model of a micro heat pipe during steady-state operation, J. Heat Transfer 116 (1994) 709–715.

[10] V. Sartre, M.C. Zaghdoudi, M. Lallemand, Effect of interfacial phenomena on evaporative heat transfer in micro heat pipes, Int. J. Therm. Sci. 39 (2000) 498–504.

[11] S. Launay, V. Sartre, M. Mantelli, K.V. De Paiva, M. Lallemand, Investigation of a wire plate micro heat pipe array, Int. J. Therm. Sci. 43 (2004) 499–507.

[12] A. Faghri, Heat Pipe Science and Technology, Taylor & Francis, London, 1995.

[13] H.B. Ma, G.P. Peterson, X.J. Lu, The influence of vapour–liquid interactions on the liquid pressure drop in triangular grooves, Int. J. Heat Mass Transfer 37 (1994) 2211–2219.

[14] G.E. Schneider, R. DeVos, Non-dimensional analysis for the heat transport capability of axially grooved heat pipes including liquid/vapour interaction, AIAA Paper No. 80-0214, 1980, pp. 1–9.

[15] V.P. Carey, Liquid–vapor phase-change phenomena, Taylor & Francis, London, 1992.

[16] P.C. Stephan, C.A. Busse, Analysis of the heat transfer coefficient of grooved heat pipe evaporator walls, Int. J. Heat Mass Transfer 35 (1992) 383–391.

[17] M. Maerefat, S. Fujikawa, T. Akamatsu, T. Goto, T. Mizutani, An experimental study of non-equilibrium vapour condensation in a shock-tube, Exp. Fluids 7 (1989) 513–520.